

2017-03-15

Hydrothermal cooling of the ocean crust: Insights from ODP Hole 1256D

Harris, Michelle

<http://hdl.handle.net/10026.1/8542>

10.1016/j.epsl.2017.01.010

Earth and Planetary Science Letters

Elsevier BV

All content in PEARL is protected by copyright law. Author manuscripts are made available in accordance with publisher policies. Please cite only the published version using the details provided on the item record or document. In the absence of an open licence (e.g. Creative Commons), permissions for further reuse of content should be sought from the publisher or author.

"This is an accepted manuscript of an article published by Elsevier in *Earth and Planetary Science Letters* 2017 available at:
<http://dx.doi.org/10.1016/j.epsl.2017.01.010>"

Please cite this article as: Harris, M., Coggon, R.M., Wood, M., Smith-Duque, C.E., Henstock, T.J & Teagle, D.A.H. Hydrothermal cooling of the ocean crust: Insights from ODP Hole 1256D, *Earth and Planetary Science Letters* (2017) 462, 110-121

1 Hydrothermal cooling of the ocean crust: Insights from ODP Hole 1256D

2

3 Michelle Harris^{*1, 2}

4 Rosalind M. Coggon¹

5 Martin Wood¹

6 Christopher E. Smith-Duque¹

7 Timothy J. Henstock¹

8 Damon A.H. Teagle¹

9

10

11 ¹ Ocean and Earth Science, National Oceanography Centre Southampton, University
12 of Southampton, European Way, Southampton, SO14 3ZH, UK

13 ² current address: School of Geography, Earth and Environmental Sciences, Plymouth
14 University, Plymouth, PL4 8AA, UK

15

16 * Corresponding author

17 michelle.harris@plymouth.ac.uk

18 +441752 584551

19 **Abstract (363 words)**

20 The formation of new ocean crust at mid-ocean ridges is a fundamental component of
21 the plate tectonic cycle and involves substantial transfer of heat and mass from the
22 mantle. Hydrothermal circulation at mid-ocean ridges is critical for the advection of
23 latent and sensible heat from the lower crust to enable the solidification of ocean crust
24 near to the ridge axis. The sheeted dike complex (SDC) is the critical region between
25 the eruptive lavas and the gabbros through which seawater-derived recharge fluids
26 must transit to exchange heat with the magma chambers that form the lower ocean
27 crust.

28

29 ODP Hole 1256D in the eastern equatorial Pacific Ocean provides the only
30 continuous sampling of in-situ intact upper ocean crust formed at a fast spreading
31 rate, through the SDC into the dike-gabbro transition zone. Here we exploit a high
32 sample density profile of the Sr-isotopic composition of Hole 1256D to quantify the
33 time-integrated hydrothermal recharge fluid flux through the SDC. Assuming
34 kinetically limited fluid-rock Sr exchange, a fluid flux of $1.5\text{-}3.2 \times 10^6 \text{ kgm}^{-2}$ is
35 required to produce the observed Sr-isotopic shifts. Despite significant differences in
36 the distribution and intensity of hydrothermal alteration and fluid/rock Sr-isotopic
37 exchange between Hole 1256D and SDC sampled in other oceanic environments
38 (ODP Hole 504B, Hess Deep and Pito Deep), the estimated recharge fluid flux at all
39 sites are similar, suggesting that the heat flux extracted by the upper crustal axial
40 hydrothermal system is relatively uniform at intermediate to fast spreading rates.

41

42 The hydrothermal heat flux removed by fluid flow through the SDCs, is sufficient to
43 remove only ~20 to 60% of the available latent and sensible heat from the lower crust.
44 Consequently, there must be additional thermal and chemical fluid-rock exchange
45 deeper in the crust, at least of comparable size to the upper crustal hydrothermal
46 system. Two scenarios are proposed for the potential geometry of this deeper
47 hydrothermal system. The first requires the downward expansion of the upper crustal
48 hydrothermal system ~800 m into the lower crust in response to a downward
49 migrating conductive boundary layer. The second scenario invokes a separate
50 hydrothermal system in the lower crust for which fluid recharge bypasses reaction
51 with the sheeted dikes, perhaps via flow down faults.

52

53 **Keywords**

54 Ocean crust; hydrothermal; Sr isotopes; heat flux

55

56 **Hydrothermal cooling of the ocean crust: Insights from ODP Hole 1256D**

57

58 **Harris et al., submitted to EPSL (December 2016).**

59

60 **Highlights:**

61

- 62 • ODP Hole 1256D provides a high-density sampling of upper fast-spread
63 oceanic crust.
- 64
- 65 • Sr isotopes record the hydrothermal recharge flux through Hole 1256D
66 sheeted dikes.
- 67
- 68 • The recharge flux ($1.5\text{-}3.2 \times 10^6 \text{ kgm}^{-2}$) is insufficient to solidify the lower
69 crust.
- 70
- 71 • Hydrothermal exchange may extend for ~800 m below the dike-gabbro
72 transition; or
- 73
- 74 • Recharge fluids may bypass the upper crust via faults to exchange heat with
75 gabbro.
- 76

77 **1. Introduction**

78 Hydrothermal circulation is a key process in the formation and evolution of the ocean
79 crust and impacts the broader Earth system through the modification of seawater
80 chemistry and the subduction of altered ocean crust (Kelemen and Manning, 2015;
81 Palmer and Edmond, 1989). At the ridge axis, hydrothermal circulation is intimately
82 involved in the magmatic accretion of new crust through the advection of sensible and
83 latent heat (e.g., Kelemen et al., 1997). Knowledge of the hydrothermal fluid fluxes
84 and pathways through the crust are crucial to understanding the size, shape and
85 distribution of magma bodies, and the processes of magma emplacement during the
86 accretion of the ocean crust in the axial region.

87

88 The deficit between the predicted and observed conductive heat flow across the ocean
89 basins persists on average until 65 ± 10 Ma, and implicates the cooling of the ocean
90 crust by hydrothermal circulation. However, ~30% of the hydrothermal heat flux is
91 advected from crust less than 1 million years old (Stein and Stein, 1994). In the axial
92 region the magmatic heat released during the formation of the lower crust drives high-
93 temperature (up to $\sim 400^\circ\text{C}$) hydrothermal circulation, which manifests at the seafloor
94 as black-smoker vents, and transports large heat and chemical fluxes to the oceans.
95 Observations of the lower ocean crust by remote geophysical methods and drilling,
96 and from tectonic windows and ophiolites have been essential in developing our
97 understanding of the subsurface fluid/rock reactions and fluid pathways during
98 hydrothermal circulation. However, long-standing questions remain about how the
99 lower crust is cooled.

100

101 The axial high temperature fluid flux is recorded in the subsurface through the
102 fluid/rock reactions within the sheeted dike complex that form secondary minerals,
103 either in fractures or replacing primary igneous minerals. The sheeted dike complex
104 has been sampled in four locations from in-situ ocean crust formed at intermediate to
105 fast spreading rates: ODP Holes 504B and 1256D, and in the tectonic windows of
106 Hess Deep and Pito Deep (Alt et al., 1996; Barker et al., 2008; Gillis et al., 2005;
107 Wilson et al., 2006). ODP Holes 504B and 1256D sample intact ocean crust,
108 providing continuous sections through the overlying volcanic sequences and the
109 sheeted dikes, whereas at Hess and Pito Deep, local triple junction-related tectonics
110 expose the deeper levels of the upper and lower crust at the seafloor. These

111 contrasting methods of sampling the sheeted dikes yield differing perspectives. Drill
112 cores enable high resolution vertical sampling that is complemented by the two
113 dimensional but discontinuous sampling afforded in tectonic windows.

114

115 The relationship between the upper crustal hydrothermal system in the lavas and
116 dikes, and the accretion of the lower oceanic crust remains poorly constrained, despite
117 this zone being significant for the exchange of heat. Two end member models for the
118 accretion of the lower oceanic crust have been proposed; the gabbro glacier (Henstock
119 et al., 1993; Phipps Morgan and Chen, 1993; Quick and Denlinger, 1993) and the
120 multiple sills models (Boudier et al., 1996; Kelemen et al., 1997; MacLeod and
121 Yoauancq, 2000). These models have contrasting requirements for the magnitude and
122 distribution of hydrothermal circulation to extract the latent and sensible heat released
123 from the cooling and crystallisation of the lower crust. In the simplest, gabbro glacier,
124 geometry the upper crustal hydrothermal system extracts much of the heat available
125 from the lower crust, because all solidification occurs in a high-level magma
126 chamber. In contrast, the multiple sills model requires deep hydrothermal heat
127 advection to extract latent heat (Coogan et al., 2006). Hence, the thermal predictions
128 of the models can be evaluated by quantifying the hydrothermal fluid flux through the
129 sheeted dike complex that is driven by heat supplied from the lower crust.

130

131 Global hydrothermal fluid fluxes have been estimated directly through the
132 extrapolation of modern vent fluxes (e.g., Baker et al., 1996) and indirectly from
133 oceanic chemical budgets (e.g., Sr, Mg; Elderfield and Schultz, 1996; Palmer and
134 Edmond, 1989) and the thermal balance of mid-ocean ridges (e.g., Morton and Sleep,
135 1985). Another approach is through the quantification of the total fluid/rock exchange
136 that occurs between seawater and ocean crust during hydrothermal circulation using
137 Sr isotopes as a tracer (Barker et al., 2008; Bickle and Teagle, 1992; Gillis et al.,
138 2005; Teagle et al., 2003). The Hole 1256D and 504B whole rock $^{87}\text{Sr}/^{86}\text{Sr}$ profiles
139 through the volcanic sequence and sheeted dike complex reveal clear differences in
140 the distribution and intensity of Sr isotope exchange. Hole 1256D shows only limited
141 seawater strontium exchange in the lavas but extensive isotopic re-equilibration in the
142 sheeted dikes. In contrast, Hole 504B exhibits significant exchange in the lavas, but
143 only slight $^{87}\text{Sr}/^{86}\text{Sr}$ increases in most of the dike section (Harris et al., 2015). These
144 profiles may reflect significant differences in the timing and intensity of hydrothermal

145 alteration and affect the global seawater-basalt exchange fluxes calculated for some
146 elements.

147

148 In this paper we will investigate whether the contrasting extent of Sr-isotopic
149 exchange in the sheeted dikes reflects different amounts of hydrothermal fluid
150 recharge. We use the high sample density Sr isotope profile of ODP Hole 1256D
151 (Harris et al., 2015) as a record of seawater-basalt exchange during hydrothermal
152 recharge, to calculate the time integrated fluid flux through the sheeted dike complex.
153 This fluid flux is compared to those calculated from the sheeted dike complex in Hole
154 504B, Hess Deep and Pito Deep to evaluate previous suggestions that hydrothermal
155 recharge fluxes are uniform in sheeted dike complexes formed at intermediate to fast
156 spreading rates (Barker et al., 2008). Our fluid flux is then converted into a
157 hydrothermal heat flux to evaluate the thermal budgets implied by contrasting models
158 of ocean crust accretion.

159

160 2. **Geological setting**

161 ODP Hole 1256D is located in the eastern equatorial Pacific and is the only complete
162 sampling of intact in-situ upper oceanic crust down to the dike/gabbro transition
163 (Figure 1; Teagle et al., 2006; Teagle et al., 2012; Wilson et al., 2006). Site 1256
164 formed at the East Pacific Rise 15 myr-ago during an interval of superfast spreading
165 (>200 mm/yr full rate; Wilson, 1996) . The ocean crust at Site 1256 is covered by 250
166 m of sediments and Hole 1256D samples 750 m of extrusive volcanic rocks, a thin
167 mineralized lava-dike transition, 350 m of sheeted dikes, and 120 m into the
168 dike/gabbro transition where two thin gabbro sills are intruded into contact
169 metamorphosed sheeted dikes (Teagle et al., 2006; Teagle et al., 2012; Wilson et al.,
170 2006).

171

172 The assemblages of secondary minerals document a downhole transition from low
173 temperature phases (e.g., clays, oxyhydroxides, carbonates) in the volcanic sequence
174 to greenschist facies phases (e.g., chlorite, actinolite, albite) in the sheeted dike
175 complex (Alt et al., 2010). This alteration is broadly similar to the only other
176 penetration of intact in-situ upper ocean crust drilled in Hole 504B (Alt et al., 1996).
177 Studies of tectonic windows also record greenschist facies alteration in the sheeted
178 dike complex, although at Pito Deep amphibole dominates the alteration assemblage

179 (Heft et al., 2008) whereas at Hess Deep chlorite is more dominant (Gillis et al.,
180 2005). Careful inspection of the Hole 1256D drill core and thin sections allows the
181 classification of dike samples into: background alteration, alteration patches and vein
182 halos, and dike margin categories. In the dike/gabbro transition early amphibole
183 alteration is overprinted by granulite facies contact metamorphism and later lower
184 temperature hydrothermal alteration at greenschist facies conditions and below (Alt et
185 al., 2010).

186

187 The whole rock Sr isotope profile of Hole 1256D records the evolution of fluid
188 pathways in the hydrothermal system and shows distinct variation between the main
189 stratigraphic sequences (Figure 1; Harris et al., 2015). The volcanic sequence has
190 limited increases in $^{87}\text{Sr}/^{86}\text{Sr}$ except along brecciated horizons and the margins of
191 anomalously thick massive flows. This suggests that the hydrothermal recharge fluid
192 reaching the top of the sheeted dikes had undergone only minor modification from
193 seawater $^{87}\text{Sr}/^{86}\text{Sr}$. Large increases in $^{87}\text{Sr}/^{86}\text{Sr}$ in the lava-dike transition are restricted
194 to mineralized, brecciated horizons and reflect the sub-surface mixing of upwelling
195 and downwelling fluids.

196

197 The sheeted dike complex provides pathways for both down-welling recharge fluids
198 and upwelling hydrothermal discharge (Harris et al., 2015), and dikes display strongly
199 elevated $^{87}\text{Sr}/^{86}\text{Sr}$ towards our estimated end member hydrothermal fluid composition,
200 indicating extensive fluid/rock exchange at greenschist facies conditions (Figure 1).
201 The Sr-isotopic composition of the upwelling hydrothermal fluid is estimated from
202 analyses of hydrothermal epidote (n=5) that precipitated in veins and alteration
203 patches. Epidote is selected as it has high Sr concentrations (>500 ppm) so is robust to
204 overprinting, and it is commonly associated with subsurface black smoker-like
205 mineralization (e.g., Bickle and Teagle, 1992). Crucially the five epidotes analysed,
206 which were sampled from the sheeted dike complex and the dike-gabbro transition,
207 record a very limited range of fluid Sr-isotopic compositions ($^{87}\text{Sr}/^{86}\text{Sr}_{\text{EPIDOTE}} =$
208 $0.70505\text{-}0.70525$, Harris et al., 2015). Although the $^{87}\text{Sr}/^{86}\text{Sr}$ composition of these
209 epidotes is higher than modern hydrothermal fluids sampled at intermediate to fast
210 spreading rates ($^{87}\text{Sr}/^{86}\text{Sr}_{\text{mean}} \sim 0.7038$; Bach and Humphris, 1999), the range is
211 consistent with the extrapolation of the observed relationship between fluid
212 composition and spreading rate to the superfast spreading rate of Site 1256 (200-220

213 mm/yr; Bach and Humphris, 1999). This approach predicts vent fluid $^{87}\text{Sr}/^{86}\text{Sr}$ of
214 0.7051-0.7056.

215

216 The dike margins generally record higher $^{87}\text{Sr}/^{86}\text{Sr}$ relative to dike cores, and provided
217 preferential recharge and discharge fluid channels through the sheeted dike complex.
218 Hydrothermal circulation through the dike complex is therefore spatially and
219 temporally variable. The dike/gabbro transition is characterized by elevated $^{87}\text{Sr}/^{86}\text{Sr}$
220 along igneous contacts that were the loci for channelized fluid flow, although with
221 only minor increases in $^{87}\text{Sr}/^{86}\text{Sr}$ in the interiors of the gabbro sills (Harris et al.,
222 2015).

223

224 **3. Method**

225 Hydrothermally altered sections of ocean crust record the time-integrated effects of
226 fluid-rock reaction. The extent of fluid/rock exchange can be used to quantify the
227 magnitude of the time integrated fluid flux through the section, that is the total
228 volume of fluid that passed through a unit area of crust. Here we model the time
229 integrated fluid flux assuming one dimensional kinetically limited fluid-rock tracer
230 exchange, following (Bickle, 1992; Bickle and Teagle, 1992; see Supplementary
231 Methods). This method uses the Damköhler number, the ratio of the advective tracer
232 transport time to the perpendicular tracer exchange time, to describe the effectiveness
233 of wall rock tracer exchange. The Simplex algorithm is used to fit the Damköhler
234 number and fluid flux penetration distance to the Sr-isotopic composition of whole
235 rock and epidote mineral analyses by minimizing the root-mean-square error (Press et
236 al., 1992). These models assume hydrothermal recharge occurs regionally via porous
237 media flow or through very closely spaced fractures, whereas the upwelling black
238 smoker fluids ascend through the sheeted dike complex via concentrated discharge
239 zones (see Bickle and Teagle, 1992). We assume that exchange with the whole rock is
240 limited only by the relative rate of kinetic exchange. The mass balance assumes that
241 past seawater had the same Sr concentration as modern seawater (Table 1), and that,
242 on average, the Sr content of the reacting fluid is little changed throughout the fluid
243 flow pathway, as supported by the similar Sr concentrations of modern seawater and
244 black smoker fluids ($[\text{Sr}] = 65\text{-}257 \mu\text{mol/kg}$, (Von Damm, 1995)). The epidote and
245 rock data populations are given equal weighting in the model, regardless of their

246 differing population sizes, to force the fluid to evolve to epidote compositions at the
247 base of the model interval.

248

249 The different alteration/igneous features identified (pervasive background alteration,
250 alteration patches and halos, dike margins) represent differences in pathways and
251 extent of fluid-rock interactions (Harris et al., 2015). To investigate their potential
252 contribution to the fluid flux through Hole 1256D, the best-fit fluid fluxes and
253 Damköhler numbers are calculated for each category: background only, halos/patches,
254 dike margins, as well as the complete dataset (Table 2).

255

256 The initial $^{87}\text{Sr}/^{86}\text{Sr}$ of the rock is the primary MORB composition (0.7028; Harris et
257 al., 2015) and the final rock composition is the whole rock $^{87}\text{Sr}/^{86}\text{Sr}$ profile. Both the
258 best fit to the entire dataset (n=196), along with the best fit to 10 m averages are
259 determined. Based on the minimal change in whole rock $^{87}\text{Sr}/^{86}\text{Sr}$ in the overlying
260 volcanic sequence, the fluid entering the top of the sheeted dikes is interpreted to have
261 a composition that is little changed from 15 Ma seawater ($^{87}\text{Sr}/^{86}\text{Sr}$ 0.70875;
262 McArthur et al., 2001). The final fluid composition is represented by the estimated
263 hydrothermal fluid composition for Hole 1256D, as determined by epidote mineral
264 separates (0.70505-0.70525).

265

266 The modelled zone begins at the top of the sheeted dike complex (1060 metres below
267 seafloor) at the onset of greenschist facies alteration, and extends down to the
268 dike/gabbro transition, with a total thickness of 390 m (Figure 2). The latter is based
269 on the assumption that the base of the black smoker hydrothermal system is a narrow
270 conductive boundary layer (CBL) overlying a convecting magma chamber in the
271 uppermost gabbros. This assumption is consistent with the observed contact
272 metamorphism in the lowermost Hole 1256D sheeted dikes under granulite facies
273 conditions (Teagle et al., 2006). Thermal calculations indicate that these
274 ‘granoblastic’ dikes formed in a CBL overlying a steady state high-level axial magma
275 chamber (Koepke et al., 2008), similar to previously documented CBL in the Troodos
276 ophiolite (Gillis and Coogan, 2002). The modelled interval includes 350 m of sheeted
277 dike complex and 40 m of granoblastic dike screens that were part of the dike
278 complex and are now within the dike/gabbro transition. The granoblastic dikes have a
279 narrow range of whole rock Sr isotopic compositions, which are interpreted to have

280 been homogenized during recrystallization to record an average $^{87}\text{Sr}/^{86}\text{Sr}$ composition
281 created during hydrothermal circulation at the ridge axis (Harris et al., 2015). Late
282 stage gabbroic intrusives and minor associated felsic rocks are excluded from our
283 calculations.

284

285 **4. Results**

286 The best fit time-integrated fluid flux and Damköhler number for each modelled
287 scenario for Hole 1256D are shown in Table 2. The difference between fitting the
288 model to all data points and to 10 m downhole averages is minor (Figure 3). A
289 scenario including all the available data requires a minimum time integrated fluid flux
290 of $2.2 \times 10^6 \text{ kg m}^{-2}$ with a N_D of 0.27 (Figure 3). This Damköhler number indicates
291 partial fluid-solid exchange and is consistent with the observed partial
292 recrystallization of the dikes to greenschist facies minerals. Our high sampling density
293 allows us to evaluate the potential variability in the fluid flux and Damköhler number
294 that are associated with the different alteration regimes ($1.5\text{--}3.2 \times 10^6 \text{ kgm}^{-2}$ and N_D
295 $=0.16\text{--}0.44$, respectively; Figure 3; Table 2), confirming that although fluid/rock
296 reaction is heterogeneous within the Hole 1256D sheeted dikes, variations are
297 relatively minor.

298

299 In order to compare the results from Hole 1256D to other crustal sites in a self-
300 consistent manner, the time integrated fluid fluxes for Hole 504B, Hess Deep and Pito
301 Deep have been recalculated following the same approach (Table 2). The best-fit
302 models for Hole 504B, Hess and Pito Deep have N_D 0.09–0.19, and time-integrated
303 fluid fluxes of $1.4\text{--}2.2 \times 10^6 \text{ kgm}^{-2}$ (Table 2). These results are similar to those
304 calculated using a constant N_D of 0.1 (Barker et al., 2008).

305

306 The 95% confidence interval for the optimal solution of the time-integrated fluid flux
307 and N_D was calculated for each crustal site (Figure 4) by performing an F-test for non-
308 linear confidence intervals using the SSE for each solution. The confidence intervals
309 demonstrate that the N_D is generally better constrained than the time-integrated fluid
310 flux. The confidence intervals for the time-integrated fluid flux are variable but
311 always $<0.5 \times 10^6 \text{ kgm}^{-2}$.

312

313 **5. Discussion**

5.1. Validity of assumptions

A key assumption of this mass balance approach is that Sr is immobile during hydrothermal alteration, which is supported by the similar Sr contents of seawater and black smoker fluids (Teagle et al., 2003) and experimental fluid-rock exchange experiments (Berndt et al., 1988). However, previous studies have suggested that Sr is mobile during hydrothermal circulation and it can be lost from either the fluid or the rock (Barker et al., 2010a; Barker et al., 2008). Sr can be lost from the fluid through the recrystallization of igneous plagioclase, or through the precipitation of anhydrite, although this process remains poorly quantified (Teagle et al., 1998; Teagle et al., 2003). The variation in Sr concentrations in the hydrothermally altered samples can be compared to the predicted igneous concentration to assess whether Sr has been mobilised during hydrothermal alteration. This is complicated by the insensitivity of Sr to magmatic fractionation (Coogan and Dosso, 2012) and for Hole 1256D the magmatic composition is best estimated from the least altered samples, which have Sr concentrations in the range 60-100 ppm (Harris et al., 2015). In the sheeted dike complex only a small proportion of the samples have undergone Sr loss (8%) or Sr gain (15%), with Sr mobility predominantly restricted to alteration patches or dike margins rather than the background samples. This suggests that although there can be local mobilization of Sr, on average the bulk composition of the crust remains constant. In contrast, ~30% of background samples from Pito Deep have lost Sr (Barker et al., 2008) and a synthesis of global data indicate that black smoker fluids have elevated Sr concentrations compared to seawater (Coogan and Dosso, 2012). If the Hole 1256D dikes had undergone substantial pervasive Sr loss (> 9 ppm) similar to Pito Deep, then this would result in a decrease in the time-integrated fluid flux by $0.5 \times 10^6 \text{ kgm}^{-2}$. In contrast, the loss of Sr from the fluid due to the precipitation of anhydrite would increase the estimated fluid fluxes (Barker et al., 2008). In Hole 1256D anhydrite is present over several hundred metres and is most abundant in the lava-dike transition zone and the upper 200 m of the sheeted dike complex. It is more abundant than in Hole 504B, albeit only as a minor phase (Teagle et al., 2006). If the fluid lost 40% of its Sr through anhydrite precipitation (following Barker et al., 2008), the Hole 1256D fluid flux would increase by $1.2 \times 10^6 \text{ kgm}^{-2}$.

347 The complex transition between the upper and lower crust has been observed at Hess
348 Deep, Pito Deep and in the Troodos and Semail ophiolites (France et al., 2009; Gillis,
349 2008). Hole 1256D also shows a similar complexity of the upper-lower crust
350 transition in terms of assimilation and the migration of the axial melt lens. Such
351 migration results in uncertainty regarding the thickness of the sheeted dike complex
352 and hence the thickness of the modelled zone, which is critical for calculating the
353 fluid flux. A key result of the 1256D drilling was the successful prediction of the
354 upper crustal thickness (depth to gabbro) from the observed relationship between
355 spreading rate and the depth to seismically imaged axial melt lenses (Wilson et al.,
356 2006). Given the thickness of the volcanic sequence in Hole 1256D, the predicted
357 upper crustal thickness equates to a sheeted dike thickness of 214 - 489 m. 390 m of
358 sheeted dikes have now been cored in Hole 1256D. Increasing the model interval by
359 100 m to reflect the maximum predicted thickness of sheeted dikes increases the time-
360 integrated fluid flux by $0.3\text{--}0.7 \times 10^6 \text{ kgm}^{-2}$, where the range reflects the variable Sr-
361 isotopic compositions of background and margin samples. The potential variability in
362 the input parameters (Sr concentration, model depth) results in uncertainty in the
363 calculated fluid flux of comparable magnitude to the model confidence intervals, and
364 does not significantly impact interpretation of the fluid flux.

365
366
367

5.2. Ocean crust fluid fluxes

368 The four ocean crust sheeted dike complexes sampled to date differ primarily in their
369 thickness, with the Hole 1256D sheeted dike complex being much thinner (~400 m v
370 >1000 m) than at Hole 504B, Hess Deep and Pito Deep (Alt et al., 1996a; Barker et
371 al., 2008; Gillis et al., 2005; Wilson et al., 2006). The Sr isotope profiles for the
372 sheeted dike complexes are also different. Given the nature of the sampling at the
373 different sites, the samples from Hess and Pito Deep are most comparable to the
374 1256D background rocks. The $^{87}\text{Sr}/^{86}\text{Sr}$ profile through Hole 504B shows a decrease
375 in strontium isotope composition with depth whereas the Pito and Hess Deep profiles
376 are generally uniform with depth (Figure 5). The Sr profile for the Hole 1256D dike
377 complex records the greatest extent of fluid/rock exchange of all the profiles. This
378 difference in Sr isotopes is highlighted by normalized cumulative frequency curves
379 where the distribution for Hole 504B, Hess Deep and Pito is very similar for ~80% of
380 the population (Figure 5). However, the Hole 1256D cumulate frequency curve is

381 markedly different to the other populations, even when the more altered dike margins
382 are removed from the Hole 1256D population. The greater exchange in Sr isotopes in
383 the dikes in Hole 1256D may result from the narrow thickness of the dike complex
384 and the consequent steeper thermal gradient present, as reflected in the higher best fit
385 Damköhler number. The range of the time-integrated fluid flux for the Hole 1256D
386 sheeted dike complex ($1.5\text{--}3.2 \times 10^6 \text{ kgm}^{-2}$) is comparable to estimates from other
387 crustal locations, despite major differences in their whole rock Sr isotope profiles.
388 This result therefore suggests that although the high temperature fluid flux of the axial
389 hydrothermal system is comparable at intermediate to superfast spreading rates, the
390 distribution and intensity of the associated hydrothermal alteration and the resultant
391 chemical exchange varies between the studied crustal sections. This variability in Sr-
392 isotope exchange is also apparent for the upper crustal volcanic sequences in Hole
393 1256D and Hole 504B (Harris et al., 2015) indicating there may be a disconnect
394 between the axial recharge fluid flux and the crustal chemical budgets for certain
395 elements, especially those exchanged at lower temperatures (e.g., C, Mg, Tl, K).

396

397 The axial high temperature hydrothermal fluid flux has been estimated using a variety
398 of other geochemical tracers. Estimates based on thallium (Nielson et al., 2006) and
399 sulphur budgets (Barker et al., 2010a; Teagle et al., 1998) of $2.4\text{--}3.0 \times 10^6 \text{ kgm}^{-2}$ are
400 comparable to those calculated from Sr isotope tracer transport, whereas the estimate
401 from lithium isotopes (Chan et al., 2002) shows a much greater range ($1.3\text{--}8.7 \times 10^6$
402 kgm^{-2}), but remains a similar order of magnitude (Figure 6). In contrast, indirect
403 estimates from global geochemical budgets (e.g., Sr Palmer and Edmond, 1989) are
404 an order of magnitude larger, as are those estimated from the Troodos ophiolite
405 (Bickle and Teagle, 1992).

406

407 From the limited crustal sections available, the estimated axial high temperature
408 hydrothermal recharge fluid flux recorded by the dike rocks appears insensitive to
409 spreading rate and differences in the relative thickness of the upper crust. The overall
410 agreement between estimates of the axial high temperature fluid flux from a variety of
411 tracers and multiple study sites, along with the comparability in the temperature of
412 fluid/rock reactions, indicates a surprising uniformity of the hydrothermal system at
413 intermediate to fast spreading rates, albeit with very limited sampling. This suggests
414 that the total heat removed by axial hydrothermal circulation through the sheeted

415 dikes is also fairly uniform and can therefore be used to investigate the thermal
416 constraints of the end member models for the accretion of the ocean crust.

417

418 Some models of axial hydrothermal circulation propose that most fluid/rock reactions
419 within the sheeted dike complex occur during regional discharge (Coogan, 2008) and
420 not recharge (Bickle and Teagle, 1992), based on modelling that shows that large
421 fluxes of downwelling fluids cool the upper dikes too efficiently (Coogan, 2008;
422 Teagle et al., 2003). Consequences of the Coogan (2008) model should be the
423 transport of seawater signatures (e.g., K, Mg, O, ^{87}Sr) down to the base of the sheeted
424 dike complex. In Hole 1256D, there is little change in Mg once magmatic
425 fractionation is accounted for, and relatively light oxygen isotope compositions
426 indicate hydrothermal exchange at high temperatures in the sheeted dikes (Gao et al.,
427 2012). Similarly, the downhole variability in $\text{Fe}^{3+}/\text{Fe}_{\text{TOT}}$ through the sheeted dike
428 complex is also minimal (<15%) with no trend with depth (Rutter, 2015). B/K and
429 Cl/K ratios from the dike complex are also consistent with high temperature alteration
430 and do not record evidence of seawater (Sano et al., 2008). These profiles suggest that
431 there is little evidence for cold seawater penetrating deep into the sheeted dike
432 complex. The decrease in whole rock Sr isotopes with depth in the sheeted dike
433 complex of Hole 1256D is consistent with reaction during recharge and not discharge.

434

435 At Pito Deep evidence of focussed fluid flow has been observed in 1 m intervals over
436 a 40 m-wide fault-zone just below the lava-dike transition (Barker et al., 2010b).
437 These fault-zones are sub-parallel to the dike margins and have Sr isotope
438 compositions that are consistent with the mixing of upwelling hydrothermal fluids and
439 downwelling seawater, similar to the brecciated horizons in the lava/dike transition in
440 Hole 1256D. If the Pito Deep observations are more representative of typical
441 intermediate to fast spreading rate crust, then hydrothermal circulation in the sheeted
442 dikes may additionally occur via focussed pathways, although such zones are not
443 strongly developed in Hole 1256D beyond the dike margins. Fluid fluxes modelled
444 using the mass balance approach adopted here could therefore represent the minimum
445 amount of fluid/rock reaction in the dike complex.

446

447 **5.3. Ocean crust heat fluxes**

448 To evaluate the proposed end-member crustal accretion models, we convert the
 449 calculated hydrothermal fluid flux into a hydrothermal heat flux and compare this to
 450 the heat available from the crystallization and cooling of the sheeted dike complex
 451 and the lower ocean crust. In the following discussion we assume that no focussed
 452 fluid flow occurs in the dike complex, and consider the consequences of this for the
 453 lower crust.

454

455 5.3.1. Hydrothermal heat flux

456 The heat flux that is transported through a unit area of crust by hydrothermal fluids is
 457 given by:

$$458 \quad Q_{ht} = F \int_{T_{sw}}^{T_{ht}} C_p \cdot dT \quad (1)$$

459 where: Q_{ht} is the hydrothermal heat flux (Jm^{-2}); F is the hydrothermal fluid flux (kg
 460 m^{-2}); C_p is the specific heat capacity of the fluid ($J kg^{-1} °C^{-1}$), which is a function of
 461 temperature (T) and pressure; and T_{sw} and T_{ht} are the temperatures of seawater and the
 462 venting hydrothermal fluid, respectively. For simplicity we assume that all of the fluid
 463 flux is heated from $0°C$ up to the critical point for seawater at the base of the dikes
 464 ($440°C$ at $40 MPa$; Bischoff and Rosenbauer, 1985), consistent with maximum
 465 alteration temperatures and vent fluid temperatures (Alt et al., 2010; Von Damm,
 466 1995). The energy required to heat $1 kg$ of seawater to $440°C$ is $1.9 \times 10^6 Jkg^{-1}$
 467 (Driesner, 2007). Given our best estimate of the axial high temperature hydrothermal
 468 fluid flux at Site 1256 ($1.5\text{--}3.2 \times 10^6 kgm^{-2}$), the associated hydrothermal heat flux,
 469 calculated using Equation 4, is $2.9\text{--}6.2 \times 10^{12} Jm^{-2}$.

470

471 5.3.2. Crustal accretion heat flux

472 The axial magmatic heat flux through a unit area of crust comprises both the latent
 473 heat of crystallization and the sensible heat released during cooling, and is given by:

$$474 \quad Q_{magmatic} = \rho h [L + C_p \Delta T] \quad (2)$$

475 where: $Q_{magmatic}$ is the total magmatic heat flux (Jm^{-2}); L is the latent heat of
 476 crystallization (Jkg^{-1}); C_p is the specific heat capacity of the basalt ($Jkg^{-1}K^{-1}$); and ΔT
 477 is the axial change in temperature of the cooling basalt ($°C$).

478

479 The axial magmatic heat flux available to drive high temperature hydrothermal
 480 circulation is taken as that associated with crystallization and cooling of the sheeted

481 dike complex and the lower crust, given that the great majority of the lower crust
482 must form close to the axis in order to develop the observed prominent Moho seismic
483 reflector and transmit shear waves. In addition to the latent heat ($5 \times 10^5 \text{ Jkg}^{-1}$) (Table 1;
484 Ghiorso and Sack, 1995; Kojitani and Akaogi, 1997), close to the ridge axis the lower
485 crust must cool to subsolidus temperatures less than 1000°C releasing $1085 \text{ Jkg}^{-1}\text{K}^{-1}$
486 of specific heat. At Site 1256 the total crustal thickness is 5.0–5.5 km (Wilson et al.,
487 2003) of which the lower crust accounts for 3.75–4.25 km, given the drilled upper
488 crustal thickness of 1.25 km above the dike/gabbro transition. Assuming a density of
489 $2.9 \times 10^3 \text{ kgm}^{-3}$ (Blackman et al., 2006) for the lower crust, $7.3\text{--}8.3 \times 10^{12} \text{ Jm}^{-2}$ of heat is
490 released from crystallizing and cooling a 1 m^2 column of lower crust of this thickness
491 to 1000°C . Crystallising and cooling the sheeted dike complex releases an additional
492 $1.4 \times 10^6 \text{ Jkg}^{-1}$. The total heat released from forming both the sheeted dikes (0.4 km)
493 and the lower crust (3.75–4.25 km) at Hole 1256D is $9.5\text{--}10.6 \times 10^{12} \text{ Jm}^{-2}$. Further
494 cooling of the lower crust below 1000°C would increase this heat flux.

495

496 Our estimate of the heat transported by fluid flow through the Site 1256 upper crust
497 ($2.9\text{--}6.2 \times 10^{12} \text{ Jm}^{-2}$) is significantly less than the total heat released during formation
498 of the sheeted dikes and the lower crust ($9.5\text{--}10.6 \times 10^{12} \text{ Jm}^{-2}$). Consequently, the
499 upper crustal hydrothermal system can only account for removal of up to 29–61% of
500 the total heat that must be removed to cool and crystallise the crust at Site 1256
501 (Figure 7), based on the assertion that the lower crust will lose a only small proportion
502 of the heat flux via conductive cooling ($<10\%$; e.g., Phipps Morgan and Chen, 1993).
503 This requires additional hydrothermal circulation at Site 1256 that is not recorded by
504 the sampled sheeted dikes, but that is equal to or greater than that currently recorded
505 by the sheeted dike complex. Other study sites produce similar estimates for the total
506 heat removed by the upper crustal hydrothermal system (21-42%, Figure 7; Barker et
507 al., 2008) suggesting the observations from Hole 1256D are representative of fast to
508 intermediate spreading rate crust.

509

510

511 **5.4. Deep hydrothermal circulation**

512 Our results require that extensive hydrothermal fluid-rock exchange must occur
513 elsewhere in the crust to remove the remaining heat from the lower crust and satisfy
514 the geophysical observations that the lower crust is fully crystallized and cooled to

515 <1000°C within a few km of the ridge axis. Recent thermal models suggest that deep
516 hydrothermal circulation may occur in the lower crust if it is sufficiently permeable
517 (Theissen-Krah et al., 2016). We propose two possible scenarios for the geometry of
518 this hydrothermal system that are thermally viable to make predictions of the
519 anticipated $^{87}\text{Sr}/^{86}\text{Sr}$ profile of Hole 1256D when it is extended into cumulate
520 gabbros: (1) a larger upper crustal hydrothermal system that extends down into the
521 lower crust; and (2) the presence of a separate hydrothermal system in the lower crust
522 for which recharge fluids have by-passed reaction with the sheeted dikes (Figure 8).

523

524 Scenario 1 implies that the existing hydrothermal system in the sheeted dikes
525 represents only the uppermost portion of a larger continuous hydrothermal system that
526 has penetrated deeper into the gabbros in response to a downward migrating CBL.
527 The tracer transport method can be used to estimate the total depth of this
528 hydrothermal system by using the total fluid flux necessary to extract all of the
529 available heat from the crust. The total hydrothermal fluid flux (heating the fluid to
530 $\sim 440^\circ\text{C}$, following section 5b) needed for Hole 1256D is $5.0\text{--}5.4 \times 10^6 \text{ kgm}^{-2}$. Using
531 the previous constraints (Section 3), the tracer transport model is iteratively solved by
532 increasing the depth of the model until the required hydrothermal fluid flux is
533 achieved. For Hole 1256D the total required depth for the hydrothermal system is
534 1050–1190 m, indicating that fluid circulation must penetrate a further 660 to 800 m
535 into the gabbros (Figure 8).

536

537 Scenario 2 proposes the existence of an additional hydrothermal system in the lower
538 crust, and critically, that fluid recharge has by-passed fluid/rock reaction with the
539 sheeted dikes sampled in Hole 1256D. This could be achieved by focused fluid flow
540 through the upper crust, perhaps along faults (Coogan et al., 2006) or in a restricted
541 downwelling zone (Figure 8; Tolstoy et al., 2008). The size of this hydrothermal
542 system can be estimated from the total heat flux available, the upper crustal heat flux
543 that is removed, and by considering the potential temperature of fluids in the lower
544 crust. The distribution of this fluid flux in the lower crust and the extent of fluid/rock
545 exchange are highly speculative. As a starting point we consider the minimum amount
546 of lower crust that would have to be in equilibrium with the hydrothermal fluid in
547 order to account for the heat flux deficit, assuming the fluid entered the lower crust as
548 cold seawater and evolved into hydrothermal fluids with compositions comparable to

549 those in the sheeted dike complex. For a direct comparison to the upper crust, if the
550 fluid reaches ~440°C (following section 5b), 69-150 m of lower crust would need to
551 be in equilibrium with the hydrothermal fluid. If the fluid was heated to ~470°C at
552 500 bar (a more realistic pressure, heat required = $2.1 \times 10^6 \text{ J kg}^{-1}$, (Driesner, 2007)), it
553 would be recorded as 66-139 m of lower crust in Sr-isotopic equilibrium with the
554 hydrothermal fluid (Figure 8).

555

556 The lower crust has been sampled at tectonic windows and ophiolites and these
557 provide some insight into the potential lower crustal hydrothermal system and the
558 viability of the two scenarios suggested for Hole 1256D. The uppermost (800 m)
559 lower crust sampled at Hess Deep comprises pervasively altered gabbroic rocks with
560 lateral variability in mineral assemblages from amphibolite to greenschist facies
561 (Kirchner and Gillis, 2012), reminiscent of our Scenario 1. Mg-in-plagioclase cooling
562 rate estimates for the uppermost gabbros suggest rapid cooling rates (0.01-0.1 °C/yr)
563 commensurate with intense hydrothermal cooling (Faak et al., 2015). However, whole
564 rock $^{87}\text{Sr}/^{86}\text{Sr}$ are only slightly elevated relative to MORB indicating these gabbros
565 have undergone minor fluid/rock reaction, similar to the central portions of the
566 gabbroic intrusions sampled in Hole 1256D that exhibit only minor Sr isotope
567 exchange (Harris et al., 2015). Tonalite samples from Hess Deep do have elevated Sr
568 isotope compositions (0.7038) compared to the host gabbro, as observed in Hole
569 1256D. However, no zones of extensive Sr isotope exchange are recorded in the
570 gabbroic rocks from Hess Deep, in contrast to Hole 1256D, where restricted zones
571 associated with igneous contacts yield Sr-isotope ratios similar to the proposed
572 hydrothermal end member (Harris et al., 2015) and appear to be fluid conduits.
573 Kirchner and Gillis (2012) consider the uppermost plutonics to form part of the upper
574 crustal hydrothermal system (similar to scenario 1) and calculate a fluid flux of $2.1 -$
575 $2.5 \times 10^6 \text{ kg m}^{-2}$, However, this is insufficient to remove the heat available from the
576 lower crust, and requires additional hydrothermal cooling. For scenario 1 to be valid
577 we predict that the Sr-isotopic compositions of the upper ~700-800 m of gabbros at
578 Site 1256 will be strongly altered towards our estimated hydrothermal fluid ($^{87}\text{Sr}/^{86}\text{Sr}$
579 ~0.705). If this is not observed, some focused fluid recharge must bypass the sheeted
580 dike complex (scenario 2).

581

582 Evidence for focused fluid flow in the lower crust, like that proposed for scenario 2,
583 has been observed in the Semail ophiolite in Oman where 10–50 m-wide alteration
584 zones occur at ~1 km spacings in gabbros (Coogan et al., 2006). These zones are
585 associated with strong hydrothermal alteration, high vein intensities and record fluid-
586 rock exchange and mineral precipitation from amphibolite down to lower greenschist
587 facies conditions (Coogan et al., 2006). The estimated fluid flux through these
588 focused zones are an order of magnitude greater than the fluid flux through the Oman
589 sheeted dike complex. If present, such features could account for the lower crust heat
590 flux deficit apparent in Hole 1256D, assuming that the hydrothermal alteration of
591 Semail ophiolite is an appropriate analogue for fast spreading ocean crust. We would
592 predict that a deepened Hole 1256D may encounter 10-100 m-wide isolated zones of
593 hydrothermally altered gabbros with strongly elevated Sr-isotope compositions. The
594 uppermost kilometre of the lower crust therefore represents a critical region for
595 assessing the hydrothermal, igneous and structural observations that will allow the
596 end member models for the lower crust to be robustly tested.

597

598 **6. Summary and Conclusions**

599 The Sr-isotope profile through the sheeted dikes at ODP Site 1256 is significantly
600 different from those previously sampled in Hole 504B and the Hess Deep and Pito
601 Deep tectonic windows (Harris et al., 2015). In contrast to the MORB-like profiles
602 from these latter three sections, the $^{87}\text{Sr}/^{86}\text{Sr}$ of the dikes in Hole 1256D are strongly
603 elevated from MORB values (~0.7028) towards the estimated composition of the Site
604 1256 black smoke-type hydrothermal fluid (~0.705), indicating a much greater extent
605 of fluid-rock Sr-isotope exchange (Figure 5). We have applied tracer transport mass
606 balance to the high density $^{87}\text{Sr}/^{86}\text{Sr}$ profile of the Hole 1256D sheeted dike complex
607 to quantify the high temperature axial fluid flux resulting from pervasive fluid
608 recharge through the sheeted dikes to be $1.5\text{--}3.2 \times 10^6 \text{ kgm}^{-2}$. Despite the different
609 extents of Sr-isotope exchange, given the different thicknesses of the sheeted dike
610 complexes (Hole 1256D ~400 m; Hess, ~600m; 504B, Pito ~1000 m), the time-
611 integrated fluid flux through Hole 1256D is similar to those estimated from the other
612 sites (Teagle et al., 2003; Barker et al., 2008), and estimates using alternative
613 geochemical tracers (e.g., Li, Tl, S). This suggests that the axial recharge flux through
614 the sheeted dikes is remarkably uniform at intermediate to superfast spreading rates.

615 This estimate of high temperature upper crustal hydrothermal fluid flux is sufficient to
616 remove only 29-61% of the sensible and latent heat released during crystallization and
617 cooling of the Site 1256 lower crust, and requires deeper hydrothermal circulation in
618 the lower crust to satisfy the geophysical observations of modern mid-ocean ridges.
619 Two scenarios are suggested, that can be tested by further drilling in Hole 1256D: (1)
620 that the extensive hydrothermal alteration observed in the sheeted dikes continues for
621 up to 800 m into the underlying upper gabbros, or that (2) a significant portion of
622 fluid recharge (~50%) bypasses the sheeted dikes by focused fluid flow on faults or in
623 discrete zones, and reaction with these fluids should produce 10-100 m-wide isolated
624 zones of hydrothermally altered gabbros with strongly elevated Sr-isotope
625 compositions, as are seen in some ophiolites.
626

627 **Acknowledgments**

628 This research used samples and data provided by the Ocean Drilling Program and the
 629 Integrated Ocean Drilling Program. This research was funded by NERC grants
 630 NER/T/S/2003/00048 and NE/E001971/1 to DAHT, NERC studentships to MH
 631 (NER/S/A/2005/13475A), post-cruise funding to MH (NE/L00059/1; IODP Exp 335)
 632 and rapid response funding from UK-IODP to DAHT, RMC, CSD and MH (ODP
 633 206, IODP Exp. 309/312, 335). DAHT acknowledges a Royal Society Wolfson
 634 Foundation Merit Award (WM130051) that supported this research.

635

636 Table 1: Parameters used in the Hole 1256D fluid flux models and heat flux
 637 calculations

Parameter	Value	Reference
Initial rock $^{87}\text{Sr}/^{86}\text{Sr}$	0.7028	(Harris et al., 2015)
Initial rock $[\text{Sr}] = C_s$	79 \pm 16 ppm	(Harris et al., 2015)
Initial fluid $^{87}\text{Sr}/^{86}\text{Sr}$	0.70875	(McArthur et al., 2001)
Initial fluid $[\text{Sr}] = C_f$	8 ppm	
Density of upper ocean crust (ρ_s)	2700 kg/m ³	
Density of fluid (ρ_f)	1000 kg/m ³	
Final fluid $^{87}\text{Sr}/^{86}\text{Sr}$	0.70505-0.70525	(Harris et al., 2015)
Volumetric solid/fluid partition coefficient: $K_v = \frac{\rho_f C_f}{\rho_s C_s}$	0.038	
Heat required to raise 1kg of seawater from 0 - 440°C	1.93 x 10 ⁶ J/kg	(Driesner, 2007)
Thickness of lower crust at Site 1256	3.75-4.25 km	(Wilson et al., 2003)
Full spreading rate at Site 1256D	220 mm/yr	(Wilson et al., 2003)
Latent heat crystallisation	5.06 x 10 ⁵ J/kg	(Kojitani and Akaogi, 1995)
Specific heat capacity gabbro	1085 J/kg/K	(Berman, 1988)

638

639

640

641

642

643

644

645 **Table 2:** Time integrated fluid fluxes determined from Sr-isotopic exchange

Location	Crustal age (Ma)	Full spreading rate (mm yr ⁻¹)	Model depth (m)	⁸⁷ Sr/ ⁸⁶ Sr fluid ^a	Kv	Model results ^b		Literature values ^c	
						N _D	Fluid flux (x 10 ⁶ kg m ⁻²)	N _D	Fluid flux (x 10 ⁶ kg m ⁻²)
Hole 1256D all samples	15	220	390	0.70505 – 0.70525 ^[1]	0.0375	0.25	2.2	-	-
Hole 1256D 10m averages	15	220	390	0.70505 – 0.70525 ^[1]	0.0375	0.27	2.3	-	-
Hole 1256D Background samples only	15	220	390	0.70505 – 0.70525 ^[1]	0.0375	0.16	1.5	-	-
Hole 1256D Alteration halos & patches	15	220	390	0.70505 – 0.70525 ^[1]	0.0375	0.32	2.6	-	-
Hole 1256D Dike margins	15	220	390	0.70505 – 0.70525 ^[1]	0.0375	0.44	3.2	-	-
Hole 504B	6.9	66	1035	0.7034 – 0.7038 ^[2]	0.0476	0.19	2.2	0.2 ^[3]	1.7 ^[3]
								0.1 ^[4]	2.1 ^[4]
Hess Deep	1	130	700	0.7038 – 0.7044 ^[5]	0.0329	0.09	1.4	0.1 ^[4]	1.5 ^[4]
Pito Deep	3	142	1080	0.70382 – 0.70413 ^[4]	0.0312	0.09	2.3	0.1 ^[4]	2.4 ^[4]

646
647 a: Sr isotopic composition of end-member hydrothermal fluid, constrained by epidote
648 Sr-isotope analyses; b time integrated fluid fluxes for Hole 1256D and recalculated
649 from published Sr-isotopic profiles, allowing both N_D and fluid flux to vary by
650 constraining the final fluid at the base of the system; c: previously published time
651 integrated fluid fluxes. ^[1] Harris et al., 2015; ^[2] Teagle et al., 1998; ^[3] Teagle et al., 2003; ^[4]
652 Barker et al., 2008; ^[5] Harris, unpublished data.
653

654 **Figure Captions**

655 Figure 1:

656 Location of ODP Hole 1256D on a crustal age map (5 m.yr intervals) after Wilson et
657 al., (2003 (inset) and whole rock Sr isotope profile through Hole 1256D, shown
658 relative to fresh MORB, hydrothermal fluid end member, modern day seawater and
659 15 Ma seawater (modified from Harris et al., 2015).

660

661 Figure 2:

662 Illustration of the set up for the tracer transport model used in this study, showing the
663 assumed fluid flow path through the crust in different parts of the model.

664

665

666 Figure 3:

667 Tracer transport results for Hole 1256D showing the modelled final rock and fluid
668 compositions overlain on the whole rock Sr isotope profile. Separate curves are
669 shown for background, patches and dike margins.

670

671 Figure 4:

672 Confidence region of the optimized solution based on the 2 parameters (N_D and time-
673 integrated fluid flux) for each of the study sites. The optimal solution for each case is
674 is shown by a colour coded filled circle with the surrounding ellipse representing the
675 95% confidence region, and the potential range in both N_D and fluid flux that could be
676 attained by the model.

677

678 Figure 5:

679 Cumulative frequency diagram for the extent of Sr isotope exchange in the sheeted
680 dike complexes for Hole 1256D (all, cores and margins, where cores include
681 background and patches), Hole 504B, Hess Deep and Pito Deep. Where the fraction
682 of seawater Sr is defined as:

683 Fraction seawater Sr = $(^{87}\text{Sr}/^{86}\text{Sr}_{\text{Rock}_{\text{measured}}} - ^{87}\text{Sr}/^{86}\text{Sr}_{\text{Rock}_{\text{MORB}}}) / (^{87}\text{Sr}/^{86}\text{Sr}_{\text{SW}_{\text{Sr}}} -$
684 $^{87}\text{Sr}/^{86}\text{Sr}_{\text{Rock}_{\text{MORB}}})$

685

686 Figure 6:

687 Compilation of literature estimates for the high temperature axial hydrothermal fluid
688 flux. For each estimate the range is represented by the error bar and lighter shaded
689 region, and the solid bar represents either the preferred or mid-point of the range.

690 Data and references presented in this figure are located in Supplementary Material
691 Table 1.

692

693 Figure 7:

694 Time-integrated fluid fluxes and heat fluxes for each of the crustal study sites,
695 showing the percentage of heat available from the crystallisation and cooling of the
696 sheeted dikes and lower crust that is removed by the upper crustal hydrothermal
697 system. Data presented in this figure is located in Supplementary Material Table 2.

698

699 Figure 8:

700 Illustrations of the proposed geometries of the hydrothermal system in the lower crust
701 for scenario 1 and 2, showing the predicted $^{87}\text{Sr}/^{86}\text{Sr}$ evolution of both the fluid and
702 rock. In scenario 1, the upper crustal hydrothermal system penetrates down into the
703 lower crust as the CBL migrates downwards. Scenario 2 represents a hydrothermal
704 system that has not reacted with the upper crust before reaching the lower crust. Both
705 of these scenarios could remove the necessary heat flux from crystallising and cooling
706 the lower crust.

707

708

709

710 Supplementary Material:

711 **Method in detail**

712 Hydrothermally altered profiles of ocean crust record the time-integrated effects of
713 fluid-rock reaction assuming that the crust has an approximately uniform cross
714 section. The extent of fluid/rock exchange can be used to quantify the magnitude of
715 the time integrated fluid flux through the section and represents the total volume of
716 fluid that passed through a unit area of crust (with units of $\text{m}^3 \text{m}^{-2}$, and hence
717 dimensions of length). During active hydrothermal flow the rate of tracer transport by
718 advection far exceeds the rate of tracer diffusion along the fluid flow path. Fluid flow
719 through the crust therefore results in the chromatographic displacement of a reaction
720 or isotope front, enabling the calculation of time integrated fluid fluxes from profiles
721 of geochemical tracers through hydrothermally altered rocks using tracer transport
722 mass balance (Bickle, 1992). Fluid flow is modelled as one-dimensional fluid flow
723 with tracer advection parallel to the fluid direction and also perpendicular to the fluid
724 direction via diffusion through stagnant porewater. Fluid flowing through a solid
725 matrix with interconnected porosity ϕ at a velocity of ω_o will have penetrated a
726 distance of $\omega_o t$ after time t . Since the porosity is the volume fraction occupied by the
727 fluid, the time integrated fluid flux is $\omega_o \phi t$. Assuming equilibrium exchange and that
728 the tracer is conserved, the distance that a geochemical tracer is advected through the
729 system (l) is proportional to the time integrated fluid flux ($l = K_v \omega_o \phi t$; where K_v is the
730 volumetric fluid/solid partition coefficient $[\rho_f C_f]/[\rho_s C_s]$, and ρ_f and ρ_s are the fluid
731 and solid densities, and C_f and C_s the concentrations of the tracer in the fluid and
732 solid, respectively; see Bickle and Teagle, 1992).

733

734 In geological systems fractures facilitate faster fluid flow but slower fluid-rock
735 exchange than grain boundary fluid flow because of the larger diffusion distance,
736 leading to fluid-rock disequilibrium and kinetically limited fluid-rock exchange. One
737 dimensional kinetically limited fluid-rock tracer exchange is governed by two non-
738 dimensional differential equations, describing the transport of the tracer (Equation 1;
739 derived from mass balance arguments) and the rate of fluid-rock exchange, which is
740 proportional to the difference in tracer concentration between the fluid and solid
741 (Equation 2):

742

743
$$\frac{\partial C'_s}{\partial t'} = -\Phi' \frac{\partial C'_f}{\partial t'} - \Phi' \frac{\partial C'_f}{\partial z'} \quad (1)$$

744
$$\frac{\partial C'_s}{\partial t'} = N_D(C'_f - C'_s) \quad (2)$$

745

746 where: Φ' is the ratio of the fraction of the tracer in the fluid to the fraction in the
 747 solid, per unit volume ($K_v\phi$); non-dimensional time t' is defined as $t' = \omega_0 t/h$; and
 748 non-dimensional distance z' is defined as $z' = z/h$, where z is distance in the direction
 749 of fluid flow. All of the unknown parameters in the system (fluid velocity, exchange
 750 rate of linear kinetics and time) are encompassed in the dimensionless Damköhler
 751 number (N_D):

752

753
$$N_D = \frac{\kappa h}{\omega_0} \quad (3)$$

754

755 where κ is the exchange rate for linear kinetic exchange (following Bickle, 1992). If h
 756 is taken as the fluid infiltration distance ($\omega_0 t$), then the time integrated fluid flux
 757 equals $\phi h t'$ and the Damköhler number is the ratio of the advective tracer transport
 758 time (t) to the perpendicular tracer exchange time ($1/\kappa$). The best-fit N_D provides
 759 information regarding the nature of fluid solid-exchange, where $N_D = 0$: no fluid-solid
 760 exchange occurs; $N_D = 1$: partial fluid-solid exchange occurs and the tracer front is
 761 displaced and broadened downstream of the fluid. At $N_D = \infty$ the fluid and rock are in
 762 equilibrium. The best-fit values of N_D and l , and hence time integrated fluid flux, can
 763 be determined by fitting solutions of Equations 1 and 2 to fluid and solid tracer
 764 profiles using a least-squares minimization. This approach, using Sr isotopes as the
 765 tracer, has been applied to both ophiolites (Bickle and Teagle, 1992) and modern
 766 ocean crust (Barker et al., 2008; Gillis et al., 2005; Teagle et al., 2003).

767

768 In this study we use a numerical model to calculate the fluid and rock strontium tracer
 769 profiles using Equations 1 and 2, discretized and solved using a first order upwind
 770 finite difference scheme. The Simplex algorithm is used to fit the Damköhler number
 771 and fluid flux penetration distance to the Sr-isotopic composition of whole rock and
 772 epidote mineral analyses by minimizing the root-mean-square error (Press et al.,
 773 1992). These models assume hydrothermal recharge occurs regionally via porous
 774 media flow or through very closely spaced fractures, whereas the upwelling black

775 smoker fluids ascend through the sheeted dike complex via concentrated discharge
776 zones (see Bickle and Teagle, 1992). We assume that exchange with the whole rock is
777 limited only by the relative rate of kinetic exchange. The mass balance assumes that
778 past seawater had the same Sr concentration as modern seawater, and that, on
779 average, the Sr content of the reacting fluid is little changed throughout the fluid flow
780 pathway, as supported by the similar Sr contents of modern seawater and black
781 smoker fluids ($[Sr] = 65\text{-}257 \mu\text{mol/kg}$, Von Damm, 1995). The epidote and rock data
782 populations are given equal weighting in the model, regardless of their differing
783 population sizes, to force the fluid to evolve to epidote compositions at the base of the
784 model interval.

785

786 The different alteration/igneous features identified (pervasive background alteration,
787 alteration patches and halos, dike margins) represent differences in fluid-rock
788 interactions. The dike margins were preferred fluid channels within the crust (Harris
789 et al., 2015), and alteration halos/patches represent regions of increased fluid/rock
790 exchange. To investigate their potential contribution to the fluid flux through Hole
791 1256D, the best-fit fluid fluxes and Damköhler numbers are calculated for each
792 category: background only, halos/patches, dike margins, as well as the complete
793 dataset.

794

795 The initial $^{87}\text{Sr}/^{86}\text{Sr}$ of the rock is the primary MORB composition (0.7028, Table 1,
796 (Harris et al., 2015)) and the final rock composition is the whole rock $^{87}\text{Sr}/^{86}\text{Sr}$ profile.
797 Both the best fit to the entire dataset ($n = 196$), along with the best fit to 10 m
798 averages are determined. Based on the minimal change in whole rock $^{87}\text{Sr}/^{86}\text{Sr}$ in the
799 overlying volcanic sequence, the fluid entering the top of the sheeted dikes is
800 interpreted to have a composition that is little changed from 15 Ma seawater ($^{87}\text{Sr}/^{86}\text{Sr}$
801 0.70875, Table 1). The final fluid composition is represented by the estimated
802 hydrothermal fluid composition for Hole 1256D, as determined by epidote mineral
803 separates (0.70505-0.70525, Table 1). The $^{87}\text{Sr}/^{86}\text{Sr}$ composition of the epidotes is
804 higher than modern hydrothermal fluids sampled at intermediate-fast spreading rates
805 (mean = 0.7038, (Bach and Humphris, 1999)). However the Sr isotope composition of
806 the epidotes is consistent with the extrapolation of the relationship between fluid

807 composition and spreading rate (Bach and Humphris, 1999) to the superfast spreading
808 rate of Site 1256D (220 mm/yr) that predicts vent fluids in the range of 0.7055.

809

810 The modelled zone begins at the top of the sheeted dike complex (1060 metres below
811 seafloor) at the onset of greenschist facies alteration, and extends down to the
812 dike/gabbro transition, with a total thickness of 390 m (Figure 2). The latter is based
813 on the assumption that the base of the black smoker hydrothermal system is a narrow
814 conductive boundary layer overlying a convecting magma chamber in the uppermost
815 gabbros. This depth interval includes 350 m of sheeted dike complex and 40 m of
816 granoblastic dike screens that were part of the dike complex and are now within the
817 dike/gabbro transition. The lowermost ~90 m of the sheeted dike complex are
818 recrystallized to granoblastic textures and the narrow range of their whole rock Sr
819 isotopic composition are interpreted to have been homogenized during
820 recrystallization to record an average $^{87}\text{Sr}/^{86}\text{Sr}$ profile created during hydrothermal
821 circulation at the ridge axis (Harris et al., 2015). Samples recovered during remedial
822 operations during IODP Expedition 335 are not included because of uncertainties in
823 the depth of these samples. Those samples related to late stage magmatism are also
824 excluded (Gabbro 1 and 2 and associated felsic intrusions).

825

826 **References**

827

828 Alt, J.C., Laverne, C., Coggon, R.M., Teagle, D.A.H., Banerjee, N.R., Morgan, S.,
829 Smith-Duque, C.E., Harris, M., Galli, L., 2010. Subsurface structure of a submarine
830 hydrothermal system in ocean crust formed at the East Pacific Rise, ODP/IODP Site
831 1256. *Geochemistry Geophysics Geosystems* 11, Q10010.

832 Alt, J.C., Laverne, C., Vanko, D.A., Tartarotti, P., Teagle, D.A.H., Bach, W., Zuleger,
833 E., Erzinger, J., Honnorez, J., Pezard, P.A., Becker, K., Salisbury, M.H., Wilkens,
834 R.H., 1996. Hydrothermal alteration of a section of upper oceanic crust in the Eastern
835 Equatorial Pacific: A synthesis of results from site 504 (DSDP legs 69, 70 and 83, and
836 ODP legs 111, 137, 140 and 148), in: Alt, J.C., Kinoshita, H., Stokking, L.B.,
837 Michael, P.J. (Eds.), *Proceedings of the Ocean Drilling Program, Scientific Results*,
838 148, pp. 417-434.

839 Bach, W., Humphris, S.E., 1999. Relationship between the Sr and O isotope
840 compositions of hydrothermal fluids and the spreading and magma-supply rates at
841 oceanic spreading centers. *Geology* 27, 1067-1070.

- 842 Baker, E.T., Chen, Y.J., Phipps Morgan, J., 1996. The relationship between near-axis
843 hydrothermal cooling and the spreading rate of mid-ocean ridges. *Earth and Planetary
844 Science Letters* 142, 137-145.
- 845 Barker, A.K., Coogan, L.A., Gillis, K.M., 2010a. Insights into the behaviour of
846 sulphur in mid-ocean ridge axial hydrothermal systems from the composition of the
847 sheeted dike complex at Pito Deep. *Chemical Geology* 275, 105-115.
- 848 Barker, A.K., Coogan, L.A., Gillis, K.M., Hayman, N.W., Weis, D., 2010b. Direct
849 observation of a fossil high-temperature, fault-hosted, hydrothermal upflow zone in
850 crust formed at the East Pacific Rise. *Geology* 38, 379-382.
- 851 Barker, A.K., Coogan, L.A., Gillis, K.M., Weis, D., 2008. Strontium isotope
852 constraints on fluid flow in the sheeted dike complex of fast spreading crust:
853 Pervasive fluid flow at Pito Deep. *Geochemistry Geophysics Geosystems* 9.
- 854 Berndt, M.E., Seyfried, W.E., Beck, J.W., 1988. Hydrothermal alteration processes at
855 midocean ridges: Experimental and theoretical constraints from Ca and Sr exchange
856 reactions and Sr isotopic ratios. *Journal of Geophysical Research* 93, 4573-4583.
- 857 Bickle, M.J., 1992. Transport mechanisms by fluid-flow in metamorphic rocks:
858 oxygen and strontium decoupling in the Trois Seigneurs massif - a consequence of
859 kinetic dispersion? *American Journal of Science* 292, 289-316.
- 860 Bickle, M.J., Teagle, D.A.H., 1992. Strontium alteration in the Troodos ophiolite:
861 implications for fluid fluxes and geochemical transport in mid-ocean ridge
862 hydrothermal systems. *Earth and Planetary Science Letters* 113, 219-237.
- 863 Bischoff, J.L., Rosenbauer, R.J., 1985. An equation of state for hydrothermal
864 seawater (3.2% NaCl). *American Journal of Science* 285, 725-763.
- 865 Blackman, D.K., Ildefonse, B., John, B.E., Ohara, Y., Miller, D.J., MacLeod, C.J.,
866 Scientists, E., 2006. Oceanic Core Complex Formation, Atlantis Massif.
- 867 Boudier, F., Nicolas, A., Ildefonse, B., 1996. Magma chambers in the Oman
868 ophiolite: fed from the top or the bottom? *Earth and Planetary Science Letters* 144,
869 239-250.
- 870 Chan, L.-H., Alt, J.C., Teagle, D.A.H., 2002. Lithium and lithium isotope profiles
871 through the upper oceanic crust: a study of seawater-basalt exchange at ODP Sites
872 504B and 896A. *Earth and Planetary Science Letters* 201, 187-201.
- 873 Coogan, L.A., 2008. Reconciling temperatures of metamorphism, fluid fluxes, and
874 heat transport in the upper crust at intermediate to fast spreading mid-ocean ridges.
875 *Geochemistry, Geophysics, Geosystems* 9, Q02013.

- 876 Coogan, L.A., Dosso, S., 2012. An internally consistent, probabilistic, determination
877 of ridge-axis hydrothermal fluxes from basalt-hosted systems. *Earth and Planetary*
878 *Science Letters* 323, 92-101.
- 879 Coogan, L.A., Howard, K.A., Gillis, K.M., Bickle, M.J., Chapman, H., Boyce, A.J.,
880 Jenkin, G.R.T., Wilson, R.N., 2006. Chemical and thermal constraints on focussed
881 fluid flow in the lower oceanic crust. *American Journal of Science* 306, 389-427.
- 882 Driesner, T., 2007. The system H₂O–NaCl. Part II: Correlations for molar volume,
883 enthalpy, and isobaric heat capacity from 0 to 1000°C, 1 to 5000bar, and 0 to 1
884 XNaCl. *Geochimica et Cosmochimica Acta* 71, 4902-4919.
- 885 Elderfield, H., Schultz, A., 1996. Mid-ocean ridge hydrothermal fluxes and the
886 chemical composition of the ocean. *Annu. Rev. Earth Planet. Sci.* 24, 191-224.
- 887 Faak, K., Coogan, L.A., Chakraborty, S., 2015. Near conductive cooling rates in the
888 upper-plutonic section of crust formed at the East Pacific Rise. *Earth and Planetary*
889 *Science Letters* 423, 36-47.
- 890 France, L., Ildefonse, B., Koepke, J., 2009. Interactions between magma and
891 hydrothermal system in Oman ophiolite and in IODP Hole 1256D: Fossilization of a
892 dynamic melt lense ar fast spreading ridges. *Geochemistry Geophysics Geosystems*
893 10, Q10O19, doi:10.1029/2009GC002652.
- 894 Gao, Y., Vils, F., Cooper, K.M., Banerjee, N., Harris, M., Hoefs, J., Teagle, D.A.H.,
895 Casey, J.F., Elliott, T., Laverne, C., Alt, J.C., Muehlenbachs, K., 2012. Downhole
896 variation of lithium and oxygen isotopic compositions of oceanic crust at East Pacific
897 Rise, ODP Site 1256. *Geochemistry Geophysics Geosystems* 13, Q10001.
- 898 Ghiorso, M.S., Sack, R.O., 1995. Chemical mass transfer in magmatic processes IV.
899 A revised and internally consistent thermodynamic model for the interpolation and
900 extrapolation of liquid-solid equilibria in magmatic systems at elevated temperatures
901 and pressures. *Contributions to Mineralogy and Petrology* 119, 197-212.
- 902 Gillis, K.A., Coogan, L.A., Pedersen, R., 2005. Strontium isotope constraints on fluid
903 flow in the upper oceanic crust at the East Pacific Rise. *Earth and Planetary Science*
904 *Letters* 232, 83-94.
- 905 Gillis, K.M., 2008. The roof of an axial magma chamber: A hornfelsic heat
906 exchanger. *Geology* 36, 299-302.
- 907 Gillis, K.M., Coogan, L.A., 2002. Antarctic migmatites from the roof of an ocean
908 ridge magma chamber. *Journal of Petrology* 43, 2075-2095.
- 909 Harris, M., Coggon, R.M., Smith-Duque, C.E., Cooper, M.J., Milton, J.A., Teagle,
910 D.A.H., 2015. Channelling of hydrothermal fluids during the accretion and evolution

- 911 of the upper oceanic crust: Sr isotope evidence from ODP Hole 1256D. *Earth and*
912 *Planetary Science Letters* 416, 56-66.
- 913 Heft, K.L., Gillis, K.M., Pollock, M.A., Karson, J.A., Klein, E.M., 2008. Role of
914 upwelling hydrothermal fluids in the development of alteration patterns at fast
915 spreading ridges: Evidence from the sheeted dike complex at Pito Deep.
916 *Geochemistry Geophysics Geosystems* 9, Q05O07.
- 917 Henstock, T.J., Woods, A.W., White, R.S., 1993. The Accretion of Oceanic-Crust by
918 Episodic Sill Intrusion. *Journal of Geophysical Research-Solid Earth* 98, 4143-4161.
- 919 Kelemen, P.B., Koga, K., Shimizu, N., 1997. Geochemistry of gabbro sills in the
920 crust-mantle transition zone of the Oman ophiolite: Implications for the origin of the
921 oceanic lower crust. *Earth Planet. Sci. Lett.* 146, 475-488.
- 922 Kelemen, P.B., Manning, C.E., 2015. Reevaluating carbon fluxes in subduction
923 zones, what goes down, mostly comes up. *Proceedings of the National Academy of*
924 *Sciences* 112, 3997-4006.
- 925
926 Kirchner, T.M., Gillis, K.M., 2012. Mineralogical and strontium isotopic record of
927 hydrothermal processes in the lower ocean crust at and near the East Pacific Rise.
928 *Contributions to Mineralogy and Petrology* 164, 123-141.
- 929 Koepke, J., Christie, D.M., Dziony, W., Holtz, F., Lattard, D., MacLennan, J., Park, S.,
930 Scheibner, B., Yamasaki, T., Yamazaki, S., 2008. Petrography of the dike-gabbro
931 transition at IODP Site 1256 (equatorial Pacific): The evolution of the granoblastic
932 dikes. *Geochemistry Geophysics Geosystems* 9, Q07O09.
- 933 Kojitani, H., Akaogi, M., 1997. Melting enthalpies of mantle peridotite: calorimetric
934 determinations in the system CaO-MgO-Al₂O₃-SiO₂ and application to magma
935 generation. *Earth and Planetary Science Letters* 153, 209-222.
- 936 MacLeod, C.J., Yoauancq, G., 2000. A fossil melt lens in the Oman ophiolite:
937 Implications for magma chamber processes at fast spreading ridges. *Earth and*
938 *Planetary Science Letters* 176, 357-373.
- 939 McArthur, J.M., Howarth, R.J., Bailey, T.R., 2001. Strontium isotope stratigraphy:
940 LOWESS version 3: Best fit to the marine Sr-isotope curve for 0-509 Ma and
941 accompanying look-up table for deriving numerical age. *Journal of Geology* 109, 155-
942 170.
- 943 Morton, J.L., Sleep, N.H., 1985. A mid-ocean ridge thermal model: Constraints on the
944 volume of axial hydrothermal heat flux. *Journal of Geophysical Research* 90, 11345-
945 11354.

- 946 Nielson, S.G., Rehkamper, M., Teagle, D.A.H., Butterfield, D.A., Alt, J.C., Halliday,
947 A.N., 2006. Hydrothermal fluid fluxes calculated from the isotopic mass balance of
948 thallium in the oceanic crust. *Earth and Planetary Science Letters* 251, 120-133.
- 949 Palmer, M.R., Edmond, J.M., 1989. The strontium isotope budget of the modern
950 ocean. *Earth and Planetary Science Letters* 92, 11-26.
- 951 Phipps Morgan, J., Chen, Y.J., 1993. The genesis of oceanic crust: Magma injection,
952 hydrothermal circulation and crustal flow. *Journal of Geophysical Research* 98, 6283-
953 6297.
- 954 Press, W.H., Teukolsky, S.A., Vetterling, W.T., Flannery, B.P., 1992. *Numerical
955 Recipes in C: The art of scientific computing*, 2nd ed. Cambridge University Press,
956 Cambridge.
- 957 Quick, J.E., Denlinger, R.P., 1993. Ductile Deformation and the Origin of Layered
958 Gabbro in Ophiolites. *Journal of Geophysical Research* 98, 14015-14027.
- 959 Rutter, J.E., 2015. Characterising low temperature alteration and oxidation of the
960 upper oceanic crust, Faculty of Natural and Environmental Sciences, Ocean and Earth
961 Science. University of Southampton, p. 353.
- 962 Sano, T., Miyoshi, M., Ingle, S., Banerjee, N.R., Ishimoto, M., Fukuoka, T., 2008.
963 Boron and chlorine contents of upper oceanic crust: Basement samples from IODP
964 Hole 1256D. *Geochemistry Geophysics Geosystems* 9, Q12O15.
- 965 Stein, C.A., Stein, S., 1994. Constraints on hydrothermal heat flux through the
966 oceanic lithosphere from global heat flow. *Journal of Geophysical Research* 99, 3081-
967 3095.
- 968 Teagle, D.A.H., Alt, J.C., Halliday, A.N., 1998. Tracing the chemical evolution of
969 fluids during hydrothermal recharge: Constraints from anhydrite recovered in ODP
970 Hole 504B. *Earth and Planetary Science Letters* 155, 167-182.
- 971 Teagle, D.A.H., Alt, J.C., Umino, S., Miyashita, S., Banerjee, N.R., Wilson, D.S., et
972 al., 2006. Superfast Spreading Rate Crust 2 and 3, Proceedings of the Integrated
973 Ocean Drilling Program. IODP-MI Inc., Washington, DC.
- 974 Teagle, D.A.H., Bickle, M.J., Alt, J.C., 2003. Recharge flux to ocean-ridge black
975 smoker systems: a geochemical estimate from ODP Hole 504B. *Earth and Planetary
976 Science Letters* 210, 81-89.
- 977 Teagle, D.A.H., Ildefonse, B., Blum, P., et al., 2012. Superfast Spreading Rate Crust
978 4, Proceedings of the Integrated Ocean Drilling Program. IODP-MI Inc., Tokyo.

- 979 Theissen-Krah, S., Rüpke, L.H., Hasenclever, J., 2016. Modes of crustal accretion and
980 their implications for hydrothermal circulation. *Geophysical Research Letters*,
981 2015GL067335.
- 982 Tolstoy, M., Waldhauser, F., Bohnenstiehl, D.R., Weekly, R.T., Kim, W.-Y., 2008.
983 Seismic identification of along-axis hydrothermal flow on the East Pacific Rise.
984 *Nature* 451, 181-184.
- 985 Von Damm, K.L., 1995. Controls on the Chemistry and Temporal Variability of
986 Seafloor Hydrothermal Fluids. *Geophysical Monograph*.
- 987 Wilson, D.S., 1996. Fastest known spreading on the Miocene Cocos-Pacific plate
988 boundary. *Geophysical Research Letters* 23, 3003-3006.
- 989 Wilson, D.S., Teagle, D.A.H., Acton, G.D., et al., 2003. An In Situ Section of Upper
990 Oceanic Crust Formed by Superfast Seafloor Spreading, *Proceedings of the Ocean*
991 *Drilling Program, Initial Reports*. ODP, College Station, TX.
- 992 Wilson, D.S., Teagle, D.A.H., Alt, J.C., Banerjee, N.R., Umino, S., Miyashita, S.,
993 Acton, G.D., Anna, R., Barr, S.R., Belghoul, A., Carlut, J., Christie, D.M., Coggon,
994 R.M., Cooper, K.M., Cordier, C., Crispini, L., Durand, S.R., Einaudi, F., Galli, L.,
995 Gao, Y., Geldmacher, J., Gilbert, L.A., Hayman, N.W., Herrero-Bervera, E., Hirano,
996 N., Holter, S., Ingle, S., Jiang, S., Kalberkamp, U., Kerneklian, M., Koepke, J.,
997 Laverne, C., Vasquez, H.L.L., Maclennan, J., Morgan, S., Neo, N., Nichols, H.J.,
998 Park, S.-H., Reichow, M.K., Sakuyama, T., Sano, T., Sandwell, R., Scheibner, B.,
999 Smith-Duque, C.E., Swift, S.A., Tartarotti, P., Tikku, A.A., Tominaga, M., Veloso,
1000 E.A., Yamasaki, T., Yamazaki, S., Ziegler, C., 2006. Drilling to Gabbro in Intact
1001 Ocean Crust. *Science* 312, 1016-1020.
1002

Figure 1

Click here to download [Figure: Fig1_map_Sr profile_CS5.pdf](#)

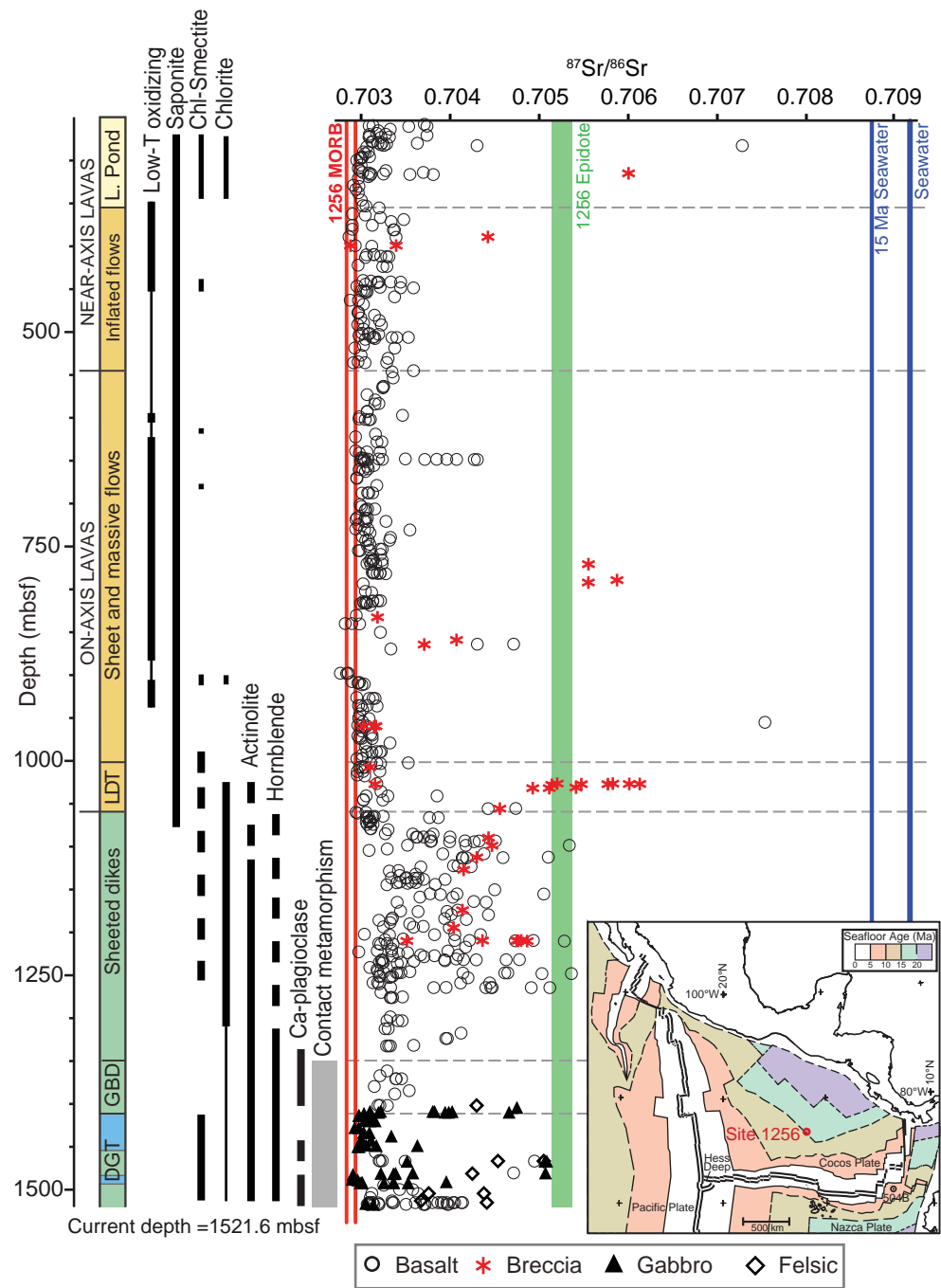


Figure 2

[Click here to download Figure: Fig2_cartoon TIFF model setup_CS5.pdf](#)

Figure 2

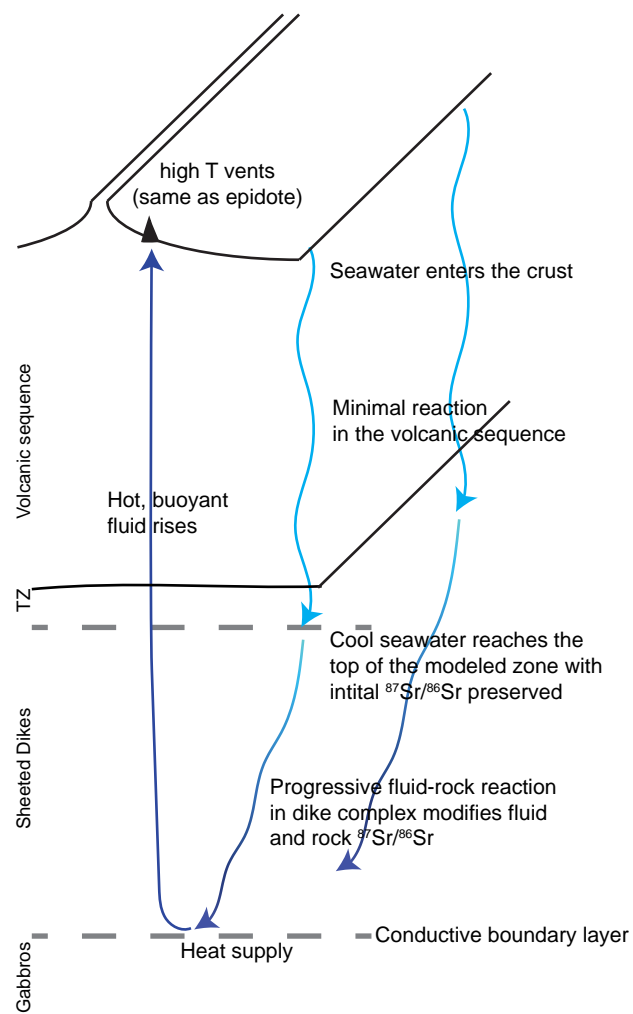


Figure 3

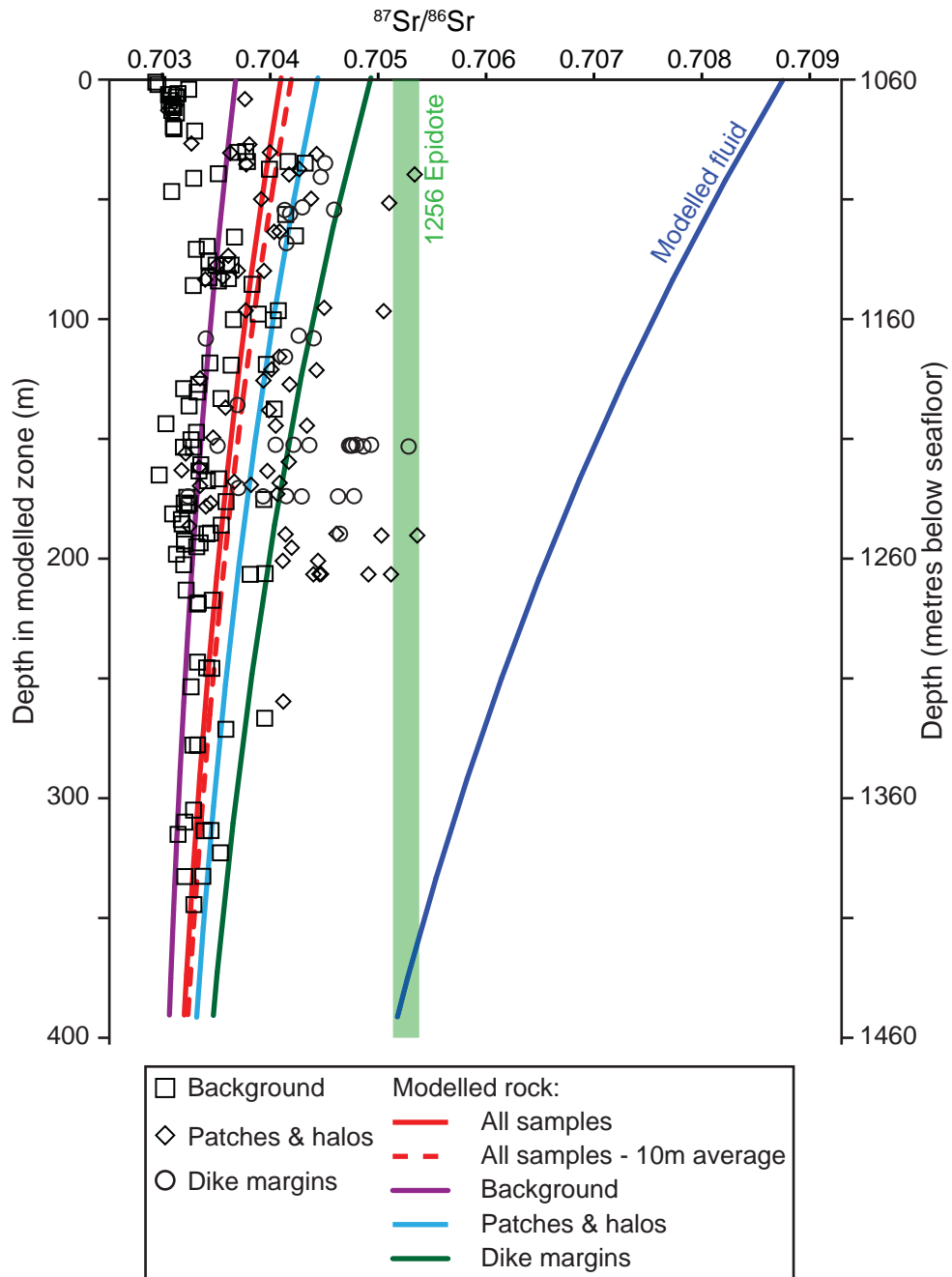


Figure 4

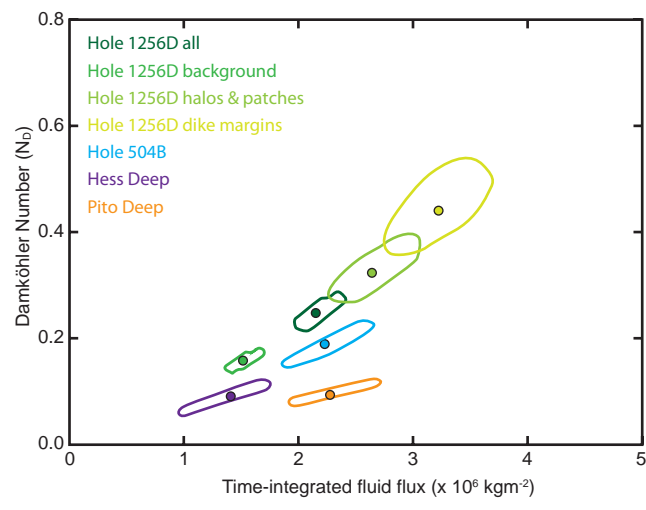


Figure 5

Figure 5

[Click here to download Figure: Fig5_Dike profile with cumulativefreq_CS5.pdf](#)

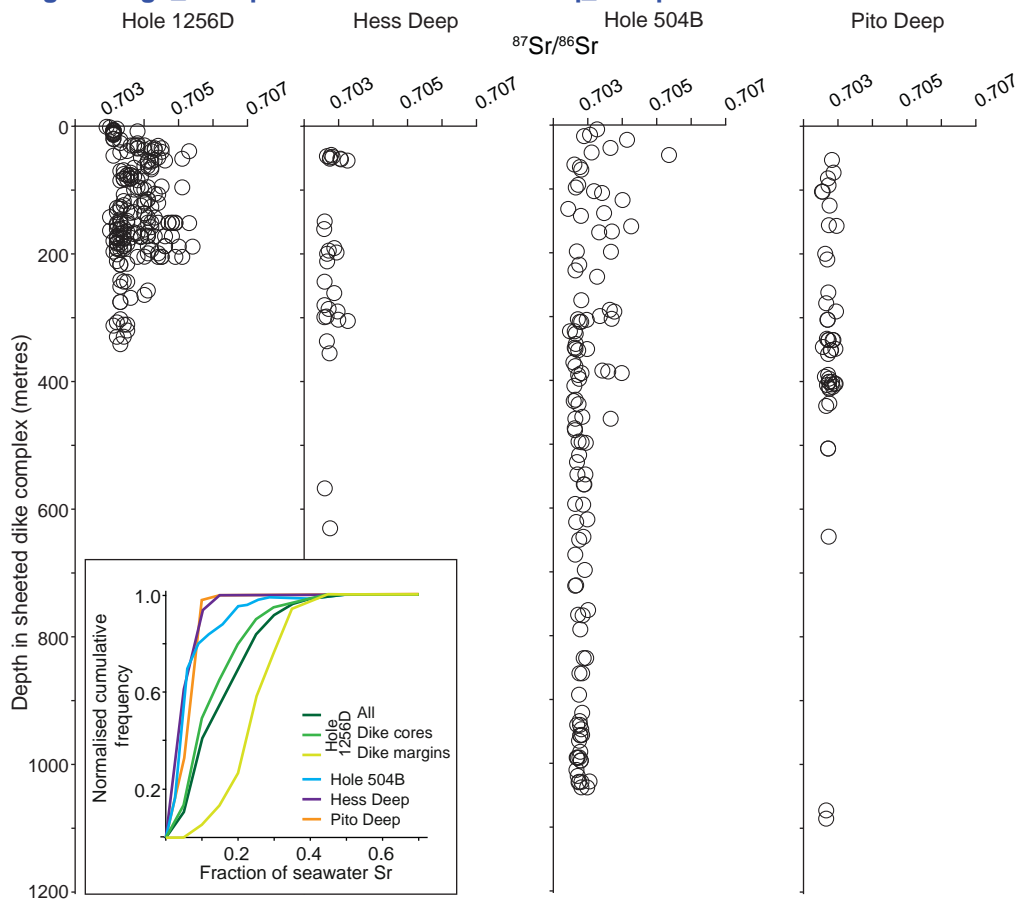


Figure 6
[Click here to download Figure: Fig6_fluid flux summary_CS5.pdf](#)

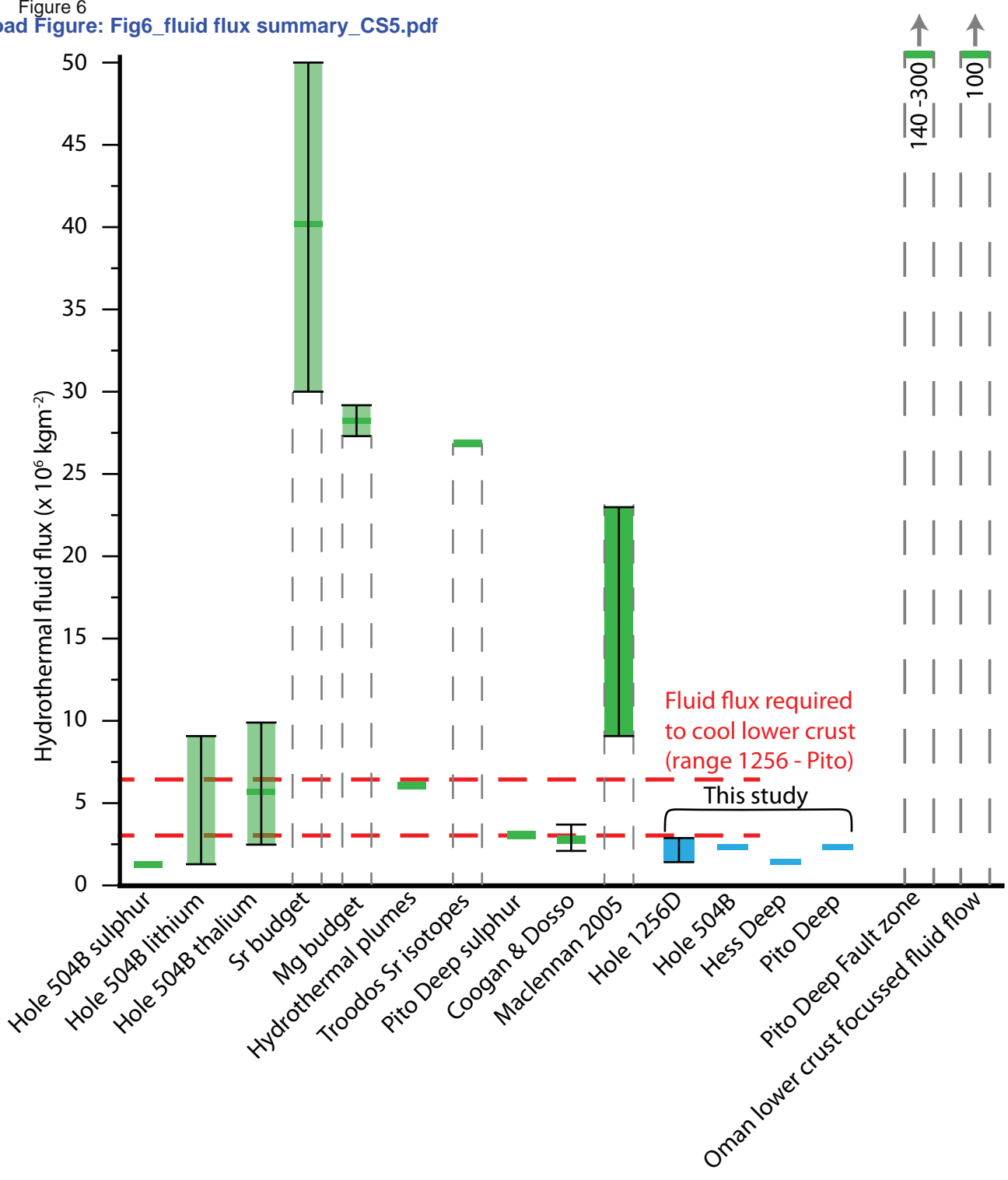


Figure 7
Figure 7

[Click here to download Figure: Fig7_heat flux summary_final_CS5.pdf](#)

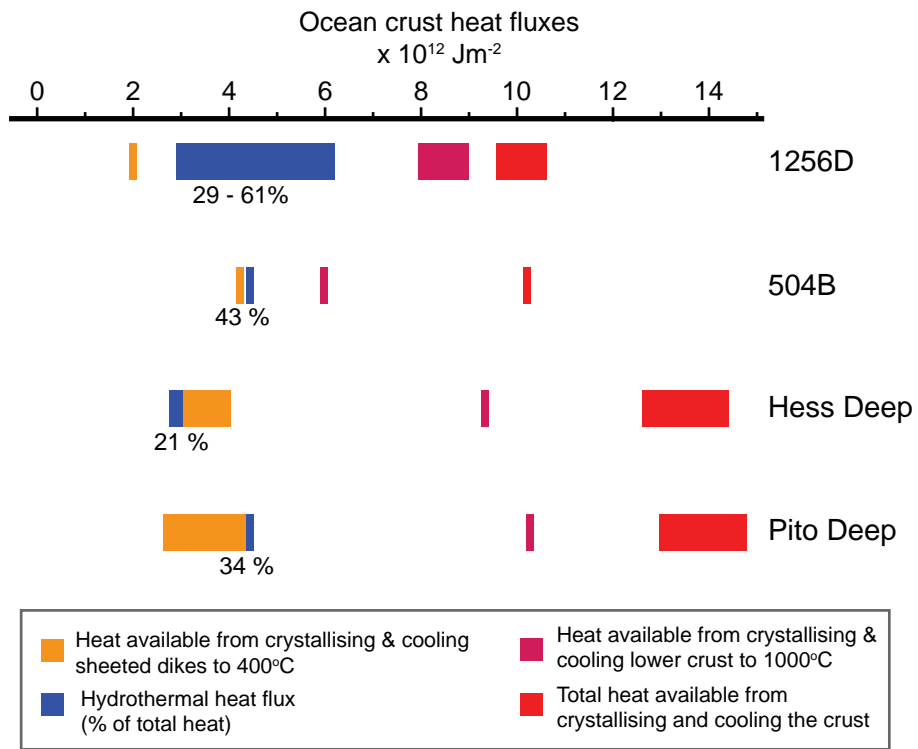
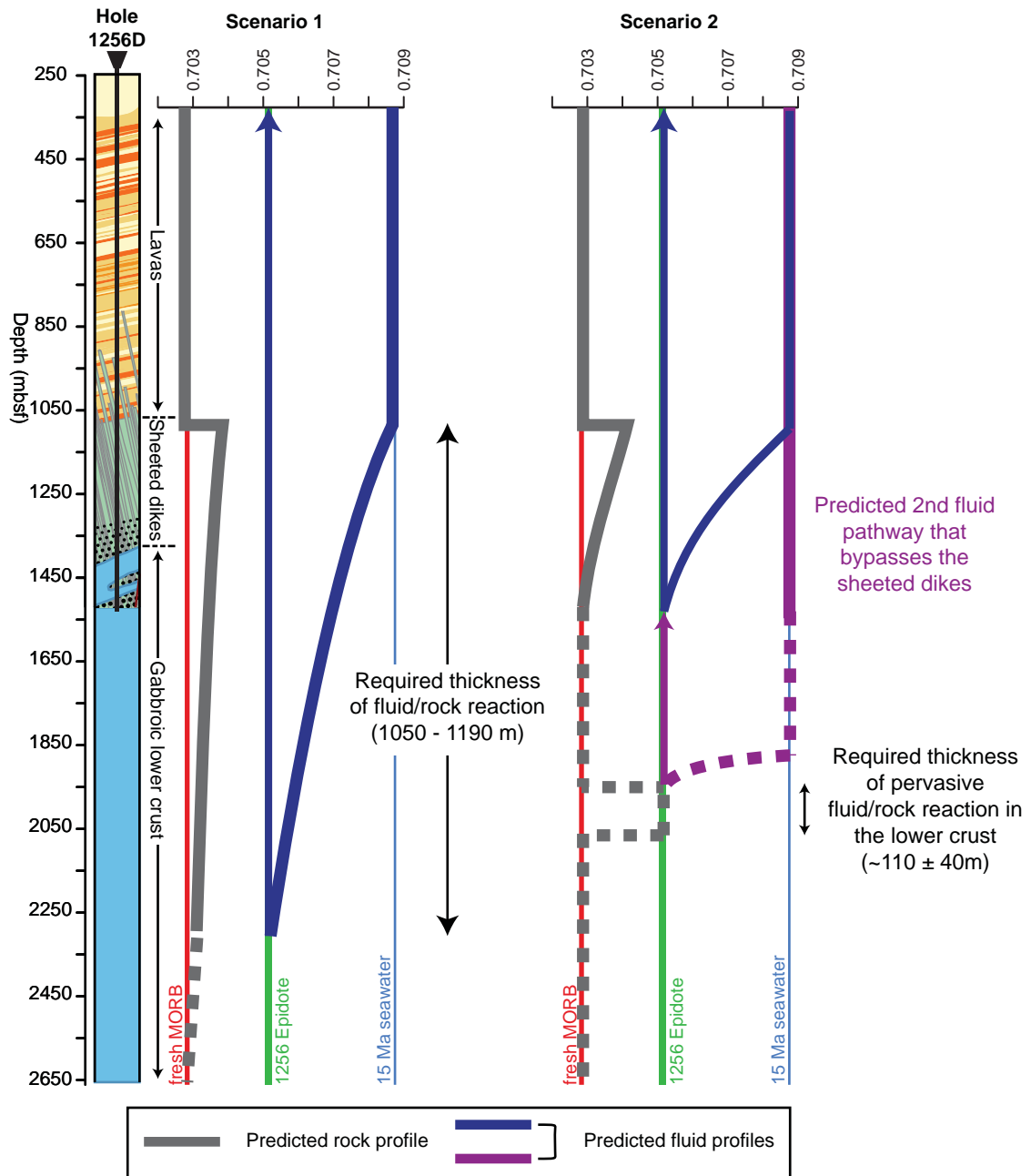


Figure 8

[Click here to download Figure: Fig8_Lower crust TIFF predictions_CS5.pdf](#)

Figure 8



Supplementary material for online publication only

[Click here to download Supplementary material for online publication only: 1256 fluid flux_Supplementary.docx](#)